

Angle-Delay Profile-Based and Timestamp-Aided Dissimilarity Metrics for Channel Charting

Phillip Stephan¹, Member, IEEE, Florian Euchner¹, Member, IEEE, Stephan ten Brink¹, Fellow, IEEE

Abstract—Channel charting is a self-supervised learning technique whose objective is to reconstruct a map of the radio environment, called channel chart, by taking advantage of similarity relationships in high-dimensional channel state information. We provide an overview of processing steps and evaluation methods for channel charting and propose a novel dissimilarity metric that takes into account angular-domain information as well as a novel deep learning-based metric. Furthermore, we suggest a method to fuse dissimilarity metrics such that both the time at which channels were measured as well as similarities in channel state information can be taken into consideration while learning a channel chart. By applying both classical and deep learning-based manifold learning to a dataset containing sub-6 GHz distributed massive MIMO channel measurements, we show that our metrics outperform previously proposed dissimilarity measures. The results indicate that the new metrics improve channel charting performance, even under non-line-of-sight conditions.

Index Terms—Channel charting, machine learning, localization, massive MIMO, manifold learning.

I. INTRODUCTION

SPATIAL multiplexing techniques like massive multiple-input multiple-output (mMIMO) are indispensable for future wide-area wireless telecommunication standards to fulfill the ever-increasing throughput demands with the limited available sub-6 GHz electromagnetic (EM) spectrum. The large number of base station (BS) antennas required for mMIMO also enable observation of the channel with high spatial resolution, facilitating additional applications including Joint Communication and Sensing (JCaS) and localization services. These applications make use of channel state information (CSI), which has to be collected at the BS for communication purposes, regardless. Classical source localization techniques such as, e.g., triangulation or multilateration, assume a channel model with line-of-sight (LoS) conditions. They tend to be inaccurate if strong multipath components disturb the direct LoS component and fail entirely under non-line-of-sight (NLoS) conditions. CSI fingerprinting-based localization methods, on the other hand, do not make any model assumptions and have been applied successfully, even in more complex environments [1] [2] [3]. However, these machine learning methods require accurate ground truth position labels, which are generally unavailable in practical systems. Channel charting, on the other hand, learns a usually two- or three-dimensional map of the radio environment, the so-called channel chart, in a self-supervised manner [4], i.e., without relying on position labels. While most of the early work on channel charting

concentrated on reconstructing local geometrical features of the radio environment [4], later work increasingly placed focus on also learning its global topology [5] [6]. The environment reconstruction is expressed as a manifold learning problem, relying on the assumption that in a sufficiently static environment, measured CSI data is mainly a function of the user equipment (UE) position and therefore lies on a low-dimensional manifold in a high-dimensional CSI feature space. Some applications of channel charting, like user localization, require global spatial consistency. For others, such as radio resource management tasks like handover prediction [7] and beam tracking [8], the accurate representation of local spatial relationships is sufficient. In this work, we aim at an accurate reconstruction of both local geometry and global topology of the environment, with a focus on comparing different novel and established dissimilarity metrics.

A. Related Work

In their seminal work on channel charting [4], C. Studer et al. suggest multiple manifold learning methods for obtaining a low-dimensional representation of high-dimensional CSI: principal component analysis (PCA) [9], Sammon’s mapping (SM) [10] and a deep learning approach using an autoencoder [11]. In contrast to the other two methods, SM does not directly process features derived from CSI, but relies on a matrix of pairwise dissimilarities between any two datapoints, forming the basis of what we call *dissimilarity metric-based* channel charting, which is the focus of this work. Their paper also coins the term *forward charting function (FCF)*, denoting the mapping from CSI feature space to low-dimensional channel chart, and establishes a distinction between two types of FCFs, namely *parametric* and *nonparametric* ones. Parametric FCFs (like aforementioned autoencoder), once learned, can map previously unseen datapoints onto an existing channel chart given the additional sample’s CSI features. Nonparametric FCFs (like SM), on the other hand, cannot trivially predict channel chart positions for points outside their training set. This makes makes parametric (i.e., usually deep learning-based) methods the preferred way to perform channel charting for many practical applications. Parametric dissimilarity metric-based channel charting was only enabled later by the proposals to employ a Siamese neural network structure [5] to parameterize SM or to use a triplet neural network based on triplet loss [12].

Besides the choice of manifold learning technique, the definition of the dissimilarity metric is crucial for the success of dissimilarity metric-based channel charting. The first

This work is supported by the German Federal Ministry of Education and Research (BMBF) within the projects Open6GHub (grant no. 16KISK019) and KOMSENS-6G (grant no. 16KISK113).

paper on channel charting [4] proposes a dissimilarity metric based on the Frobenius distance between special matrices derived from CSI. Later papers propose different metrics, some of them geometrically motivated and mathematically derived, others devised in a more ad-hoc manner based on empirical results. Notable CSI dissimilarity metric proposals include a metric derived from superresolution angular-domain information [13], a correlation matrix distance (CMD)-based metric [14], a cosine similarity (CS)-based metric [15], a metric making use of time domain CSI that we call channel impulse response amplitude (CIRA) [16] and, more recently, an angle-delay profile (ADP)-based metric [17]. In addition, [16] highlights that it is often sufficient to be able to compute dissimilarities that are indicative of local distances and that global distances, which are then called *geodesic distances*, can be computed as a combination of many local distances. In [12] and in our previous work [18], CSI-based dissimilarities were avoided entirely by using side information, namely the absolute difference in datapoint timestamps, as a metric.

While most research in channel charting is carried out on simulated channels [4][5][13][14][15][17], some authors compute channel charts for real-world measurement datasets [12][16][18]. Some previous research [13][19][20][21] specifically considers the case of *multipoint* channel charting, where CSI is available from multiple distributed BSs.

B. Contributions and Outline

After listing some limitations of our work and defining some terminology and notations, we first review our system model and present a short overview of the principles of dissimilarity metric-based channel charting in Section II. In Section III, we then introduce several commonly used dissimilarity metrics and explain our own novel metrics. Our proposals include exploiting the ADP, learning the dissimilarity metric with a neural network and fusing information from multiple existing metrics. Building on well-known classical and deep learning-based manifold learning methods summarized in Sections IV and V, respectively, and using the customary channel charting evaluation metrics given in Section VI, we compare all proposed dissimilarity metrics on a real-world dataset in Section VII. Additionally, we demonstrate that, with our novel metrics, we can get good performance even if a large portion of the dataset experiences NLoS propagation conditions. Finally, in Section VIII, we draw conclusions from the observed results and suggest some open questions for future work.

C. Limitations

To be able to provide an extensive performance comparison of many different dissimilarity metrics and manifold learning techniques, we had to constrain our evaluations to just one measurement dataset. Out of the dissimilarity metrics from literature, we had to limit ourselves to those that perform best on our dataset. Like most current channel charting work, we assume that the environment is mostly static over the duration of the data capture.

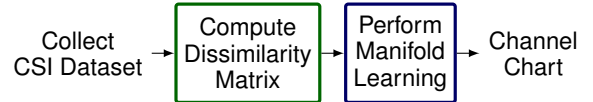


Fig. 1. The two central steps in dissimilarity metric-based channel charting

D. Terminology

In the context of channel charting, *distributed mMIMO* can be seen as an extension of *multipoint* channel charting. Whereas the latter only assumes the availability of CSI at multiple BSs, the former also ensures some additional synchronization between them. In our case, we use datasets with phase synchronization across all antennas and will therefore refer to “distributed mMIMO”, even though many of our results also apply to multipoint channel charting.

The notion of computing *dissimilarity metrics* between datapoints is common in channel charting literature. Various terms like *distance*, *similarity* or *dissimilarity metric* have been proposed to refer to this measure, but it is yet unclear which will prevail. We chose to use the expression *dissimilarity metric*, since it conveys the distinction between physical distances to dissimilarities in CSI space. Note that *metric* is used in a colloquial sense here, as not all *dissimilarity metrics* fulfill the requirements for a metric in the sense of a metric space.

E. Notations

We use boldface uppercase letters for matrices and tensors, and comma-separated subscripts for indexing. For example $\mathbf{H}_{i,j}$ refers to the entry in the i -th row and j -th column of the matrix \mathbf{H} . Boldface lowercase letters are reserved for vectors.

II. OVERVIEW: PRINCIPLES OF CHANNEL CHARTING

In a sufficiently static environment and neglecting hardware impairments and noise, CSI, which is estimated at the BS for communication purposes, is primarily determined by the location and orientation of the UE. This is the premise of channel charting, which assumes that CSI in a suitable feature space lies on a single low-dimensional manifold. The steps involved in dissimilarity metric-based channel charting are illustrated in Fig. 1: First, having collected a large CSI dataset at the BS, a *dissimilarity matrix* containing the dissimilarities between any two datapoints in the dataset is computed using a particular dissimilarity metric. Then, manifold learning is applied to obtain the FCF. The success of the second step is highly dependent on the first step, namely the choice of dissimilarity metric. Ideally, the computed dissimilarities reflect the physical distances between datapoints to a large extent. The low-dimensional representation should minimize the discrepancy between the point-to-point distances in the channel chart and the respective distances in the dissimilarity matrix. A suitable representation can be found with either classical or deep learning-based manifold learning methods. The latter implement parametric FCFs which can predict channel chart positions based on CSI input features. These input features are computed from the raw estimated CSI in a *feature engineering* step.

A. System and Data Model

In the following, we describe an abstract system model that we will employ to define dissimilarity metrics and manifold learning techniques. Refer to Section VII-A for information on the particular dataset and system used for our analyses.

We consider a mMIMO BS consisting of B distributed antenna arrays equipped with M antennas each, and a UE with a single antenna. A dataset consisting of L datapoints measured at discrete time instances $l = 1, \dots, L$ is collected, where one datapoint consists of the following parameters:

- Channel coefficients between the UE and all $B \times M$ BS antennas for N_{sub} orthogonal frequency division multiplex (OFDM) subcarriers, collected in the frequency-domain CSI tensor $\mathbf{H}^{(l)} \in \mathbb{C}^{B \times M \times N_{\text{sub}}}$. We assume that N_{sub} is even and that the subcarrier channel coefficients in \mathbf{H} are ordered such that the coefficients $\mathbf{H}_{b,m,1}^{(l)}$ correspond to the subcarrier at the center of the bandwidth (customary for discrete Fourier transform (DFT) frequency bins).
- Corresponding UE positions $\mathbf{x}^{(l)} \in \mathbb{R}^D$, measured by some reference localization system, with D being the spatial dimension (we assume $D = 2$). This information may be used for evaluation purposes.
- A timestamp $t^{(l)} \in \mathbb{R}$, measured in seconds, indicating the exact (millisecond-precision) time the CSI and position measurements were taken.

Hence, the complete dataset may be written as a set of 3-tuples $(\mathbf{H}^{(l)}, \mathbf{x}^{(l)}, t^{(l)})$ of cardinality L :

$$\text{Dataset: } \mathcal{S} = \left\{ (\mathbf{H}^{(l)}, \mathbf{x}^{(l)}, t^{(l)}) \right\}_{l=1, \dots, L}$$

For some processing steps, it may be beneficial to use a time-domain CSI representation $\tilde{\mathbf{H}}^{(l)} \in \mathbb{C}^{B \times M \times N_{\text{sub}}}$. This representation is obtained by applying the unitary inverse discrete Fourier transform to $\mathbf{H}^{(l)}$ along the frequency axis:

$$\tilde{\mathbf{H}}_{b,m,\tau}^{(l)} = \frac{1}{\sqrt{N_{\text{sub}}}} \sum_{n=1}^{N_{\text{sub}}} e^{2\pi j \cdot 1/N_{\text{sub}} \cdot (n-1) \cdot (\tau - N_{\text{sub}}/2 - 1)} \mathbf{H}_{b,m,n}^{(l)} \quad (1)$$

Note that τ in Eq. (1) is shifted such that $\tau = 1$ corresponds to the earliest and $\tau = N_{\text{sub}}$ corresponds to the last time tap.

B. Manifold Learning and Dissimilarity Metrics

Manifold learning finds a mapping from the CSI tensors $\mathbf{H}^{(l)} \in \mathbb{C}^{B \times M \times N_{\text{sub}}}$ to channel chart positions $\mathbf{z}^{(l)} \in \mathbb{R}^{D'}$, expressed by the FCF

$$\mathcal{C} : \mathbb{C}^{B \times M \times N_{\text{sub}}} \rightarrow \mathbb{R}^{D'}$$

with D' being the dimensionality of the channel chart. Subsequently, we assume $D' = D = 2$ and only consider manifold learning techniques which are based on dissimilarity metrics. A good FCF ensures that the pairwise Euclidean distance between any two mapped positions in the channel chart $\mathbf{z}^{(i)}, \mathbf{z}^{(j)} \in \mathbb{R}^{D'}$ is approximately proportional to the distances between the corresponding true UE positions $\mathbf{x}^{(i)}, \mathbf{x}^{(j)}$:

$$\|\mathbf{z}^{(i)} - \mathbf{z}^{(j)}\|_2 \propto \|\mathbf{x}^{(i)} - \mathbf{x}^{(j)}\|_2, \quad \forall i, j \in \{1, \dots, L\}.$$

In case of dissimilarity metric-based channel charting, dissimilarities computed based on a dissimilarity metric d are

considered while learning the FCF. Ideally, these dissimilarity metric should also fulfill

$$d_{i,j} \propto \|\mathbf{x}^{(i)} - \mathbf{x}^{(j)}\|_2, \quad \forall i, j \in \{1, \dots, L\}, \quad (2)$$

with $d_{i,j}$ being the computed dissimilarity between the datapoints i and j . Dissimilarities are calculated based on information that is available to the BS, such as the estimated CSI [4] [16] [15] or timestamp information [12]. A more detailed overview of different dissimilarity metrics for channel charting is given in Section III. The pairwise dissimilarities between all samples in the dataset are collected in the dissimilarity matrix

$$\mathbf{D}_{\text{pw}} = \begin{pmatrix} d_{1,1} & \cdots & d_{1,L} \\ \vdots & \ddots & \vdots \\ d_{L,1} & \cdots & d_{L,L} \end{pmatrix},$$

which is generally symmetric ($d_{i,j} = d_{j,i}$) and fulfills $d_{i,j} \geq 0 \forall i, j$ and $d_{i,i} = 0 \forall i$.

C. Feature Engineering

For deep learning-based techniques, we propose to use CSI features based on sample autocorrelations of the time-domain CSI matrices $\tilde{\mathbf{H}}^{(l)}$. These sample autocorrelations are computed for every pair b_1, b_2 of antenna array indices, for any pair m_1, m_2 of antenna indices and for every tap index τ . This way, the feature vector also contains sample correlations of antennas that are part of different antenna arrays. To this end, we define a set of index tuples \mathcal{J} as the cartesian product

$$\mathcal{J} = \{1, \dots, B\}^2 \times \{1, \dots, M\}^2 \times \{\tau_{\min}, \dots, \tau_{\max}\}.$$

Note that only time tap indices τ from τ_{\min} to τ_{\max} are taken into account, where $1 \ll \tau_{\min} < N_{\text{sub}}/2 < \tau_{\max} \ll N_{\text{sub}}$, i.e., only a few channel impulse response (CIR) taps containing the LoS path (if it exists) as well as the first few multipath components are even considered. The choice of τ_{\min} and τ_{\max} depends on the expected maximum delay spread. Since OFDM is usually operated such that the number of subcarriers N_{sub} is high enough to ensure sufficiently frequency-flat subcarriers despite the channel's frequency selectivity, the considered interval of CIR taps $\tau_{\min}, \dots, \tau_{\max}$ is small compared to the overall number of taps N_{sub} .

For each combination of indices, we compute a sample autocorrelation and collect the autocorrelations in the vector $\mathbf{c}^{(l)} \in \mathbb{C}^{B^2 M^2 (\tau_{\max} - \tau_{\min} + 1)}$:

$$\mathbf{c}^{(l)} = \left(\tilde{\mathbf{H}}_{b_1 m_1 \tau}^{(l)} \left(\tilde{\mathbf{H}}_{b_2 m_2 \tau}^{(l)} \right)^* \right)_{(b_1, b_2, m_1, m_2, \tau) \in \mathcal{J}}$$

Since we use a neural network implementation that can only handle real-valued numbers, we provide $\mathbf{c}^{(l)}$ to the network in a vectorized form with real and imaginary part separated, yielding the feature vectors

$$\mathbf{f}^{(l)} = (\text{Re} \{ \mathbf{c}^{(l)} \} \quad \text{Im} \{ \mathbf{c}^{(l)} \}) \in \mathbb{C}^{2B^2 M^2 (\tau_{\max} - \tau_{\min} + 1)}.$$

Intuitively, this means that the neural network is provided information about relative phases and powers between any two antennas in the system. Obviously, our choice of feature engineering produces very large input vectors $\mathbf{f}^{(l)}$. The feature engineering stage may be further improved, e.g., by compressing useful information in a more sparse set of features.

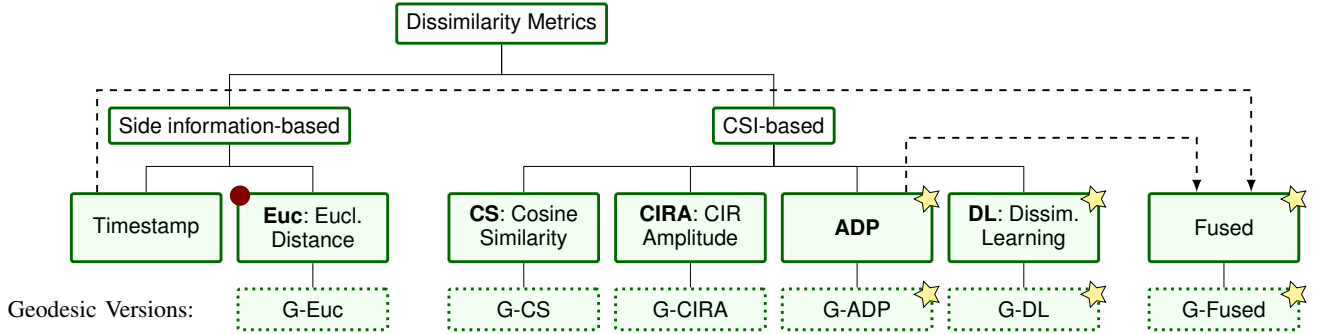


Fig. 2. Overview of dissimilarity metrics compared in this paper. Metrics marked with a star (★) are newly introduced. Metrics marked with a red circle (●) use ground truth positioning data and are only meant as baselines, not for practical implementation of a channel charting system. Note that we are considering a metric that fuses information from both ADP and timestamp metrics here, but, in general, any set of metrics may be fused into one.

III. DISSIMILARITY METRICS

A variety of dissimilarity metrics that compute pseudo-distances between measured datapoints have been proposed for channel charting. The choice of metric depends on properties of the available CSI data (e.g., number and distribution of antennas, bandwidth, phase-coherence) and the availability of side information. In general, dissimilarity metrics can be grouped into side information-based and CSI-based metrics, as illustrated in Fig. 2. Side information-based methods assume that some additional information is available at the BS in addition to wireless channel estimates. Other dissimilarity metrics are computed solely based on measured CSI. We compare the suitability of different CSI-based dissimilarity metrics from literature, namely a CS-based metric [15] and a CIRA-based metric [16], to our newly developed metric, which we refer to as ADP dissimilarity. In addition, we describe an approach where a deep neural network (DNN) learns a suitable dissimilarity metric between measured CSI, which we call dissimilarity metric learning, and we propose a method to combine information from multiple metrics.

A. Euclidean Distance (Reference System)

Under the assumption that some reference system (e.g., a global navigation satellite system (GNSS)) provides “ground truth” position labels $\{\mathbf{x}^{(l)}\}_{l=1,\dots,L}$, the Euclidean distance

$$d_{\text{Euc},i,j} = \|\mathbf{x}^{(i)} - \mathbf{x}^{(j)}\|_2$$

between these labels can be used directly as the dissimilarity metric. Obviously, this metric is unsuitable for most practical uses of channel charting, where only channel measurements at the BS are available, but is nevertheless included here as a baseline for benchmarking subsequent processing steps.

B. Absolute Time Difference

As first suggested in [12], timestamps may also reveal some information about spatial relationships between datapoints: Since the velocity of a UE is bounded, two channel measurements between BS and the same UE which are measured in quick succession are likely to be also spatially close to each other. It is reasonable to assume that timestamps are available alongside CSI measurements in practical systems.

The timestamp-based dissimilarity metric is defined as the absolute time difference between two measurements:

$$d_{\text{time},i,j} = |t^{(i)} - t^{(j)}| \quad (3)$$

Obviously, this dissimilarity metric fails to predict meaningful distances for large absolute time differences, but its usefulness has been demonstrated before [12] [18] and it can be especially powerful in combination with CSI-based metrics.

C. Channel Impulse Response Amplitude (CIRA)

A dissimilarity metric based on the CIRA was introduced in [16]. An important advantage of this metric is that phase synchronization between receivers is not required, since it only operates on CIR amplitudes, not phases. However, the metric assumes a setup with distributed receivers and is less suitable for setups with one single or few mMIMO arrays. We can apply the CIRA metric to our time-domain CIR tensors $\tilde{\mathbf{H}}^{(l)}$ as follows:

$$d_{\text{CIRA},i,j} = \sum_{b=1}^B \sum_{m=1}^M \sum_{\tau=\tau_{\min}}^{\tau_{\max}} \left| \left| \tilde{\mathbf{H}}_{b,m,\tau}^{(i)} \right| - \left| \tilde{\mathbf{H}}_{b,m,\tau}^{(j)} \right| \right| \quad (4)$$

As previously explained in Section II-C, τ_{\min} and τ_{\max} should be chosen appropriately.

D. Cosine Similarity (CS)

The use of a CS-based metric for channel charting was first proposed in [15], which assumes a narrowband system with just one mMIMO antenna array at the BS. In [15], the dissimilarity between two channel coefficient vectors $\mathbf{h}^{(i)} \in \mathbb{C}^M$ and $\mathbf{h}^{(j)} \in \mathbb{C}^M$, where M is the number of antennas in the mMIMO array, is defined as

$$d_{\text{Magoarou},i,j} = \sqrt{2 - 2 \frac{|\langle \mathbf{h}^{(i)}, \mathbf{h}^{(j)} \rangle|}{\|\mathbf{h}^{(i)}\|_2 \|\mathbf{h}^{(j)}\|_2}}$$

Empirically we determined that a slightly modified version of the metric considering the squared CS, which can be interpreted as a normalized power value, performs better with respect to all evaluation metrics:

$$d_{\text{CS-vec},i,j} = 1 - \frac{|\langle \mathbf{h}^{(i)}, \mathbf{h}^{(j)} \rangle|^2}{\|\mathbf{h}^{(i)}\|_2^2 \|\mathbf{h}^{(j)}\|_2^2}$$

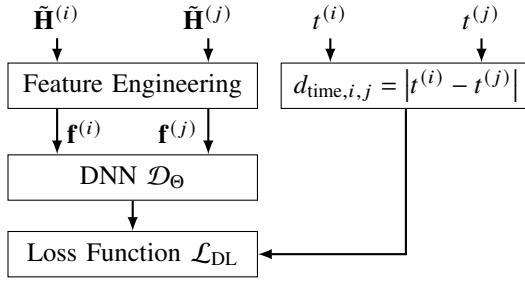


Fig. 3. Dissimilarity Metric Learning: The DNN \mathcal{D}_Θ is trained to estimate the absolute time difference between samples i, j based on their CSI.

Note that $0 \leq d_{\text{CS-vec},i,j} \leq 1$, with $d_{\text{CS-vec},i,j} = 0$ if and only if $\mathbf{h}^{(i)}$ and $\mathbf{h}^{(j)}$ are linearly dependent. We generalize this metric to wideband OFDM channels with N_{sub} subcarriers and distributed antenna setups with B antenna arrays. We achieve this by computing the summation over the dissimilarities calculated separately for each antenna array and each subcarrier:

$$d_{\text{CS},i,j} = \sum_{b=1}^B \sum_{n=1}^{N_{\text{sub}}} \left(1 - \frac{\left| \sum_{m=1}^M \left(\mathbf{H}_{b,m,n}^{(i)} \right)^* \mathbf{H}_{b,m,n}^{(j)} \right|^2}{\left(\sum_{m=1}^M \left| \mathbf{H}_{b,m,n}^{(i)} \right|^2 \right) \left(\sum_{m=1}^M \left| \mathbf{H}_{b,m,n}^{(j)} \right|^2 \right)} \right) \quad (5)$$

E. Angle-Delay Profile (ADP)

Taking inspiration from the CIRA metric in Eq. (4), we propose an enhanced version of a CS-based metric by exploiting the sparsity of time-domain CSI. Most signal power in time domain is concentrated in the LoS path (if it exists) and a few strong multipath components (MPCs). As opposed to Eq. (5), which computes cosine similarities for frequency-domain CSI data, we suggest to perform the summation over time-domain CSI matrices $\tilde{\mathbf{H}}$ for taps $\tau = \tau_{\min}, \dots, \tau_{\max}$, where τ_{\min} and τ_{\max} must be adapted to the radio environment such that all relevant MPCs are accounted for:

$$d_{\text{ADP},i,j} = \sum_{b=1}^B \sum_{\tau=\tau_{\min}}^{\tau_{\max}} \left(1 - \frac{\left| \sum_{m=1}^M \left(\tilde{\mathbf{H}}_{b,m,\tau}^{(i)} \right)^* \tilde{\mathbf{H}}_{b,m,\tau}^{(j)} \right|^2}{\left(\sum_{m=1}^M \left| \tilde{\mathbf{H}}_{b,m,\tau}^{(i)} \right|^2 \right) \left(\sum_{m=1}^M \left| \tilde{\mathbf{H}}_{b,m,\tau}^{(j)} \right|^2 \right)} \right) \quad (6)$$

Eq. (6) can be interpreted as using the angular-domain similarity in terms of power measured across multiple time-domain taps and MPCs, hence we suggest the name ADP for our novel metric. The restriction to $\tau_{\min} \leq \tau \leq \tau_{\max}$ excludes taps with weak signal and strong noise contributions (refer to Section II-C). In contrast to previously proposed angular domain metrics [13] [22], we deliberately forgo the use of superresolution techniques or the computation of earth mover's distances (EMDs), which makes computation practical for large datasets.

F. Dissimilarity Metric Learning (DL)

The previous dissimilarity metrics were explicitly defined and motivated based on assumptions grounded in the move-

ment of UEs or in EM wave propagation. However, modeling wave propagation is complicated, which makes it difficult to formulate dissimilarity metrics that adapt to all environments. In an entirely different approach, we suggest to not only use neural networks for manifold learning, but to use them to learn the dissimilarity metric itself. The architecture of the dissimilarity metric learning process is shown Fig. 3.

The challenge for this approach is the definition of a suitable loss function that does not rely on the ‘‘ground truth’’ UE positions $\mathbf{x}^{(l)}$, which must not be used. Instead, we suggest to train a DNN \mathcal{D}_Θ to estimate the absolute time difference $d_{\text{time},i,j}$ (as defined in Eq. (3)) between pairs of CSI features $\mathbf{f}^{(i)}, \mathbf{f}^{(j)}$ (as defined in Section II-C). The hope is that the predictions of \mathcal{D}_Θ may also be a useful indicator of physical distances (compare Section III-B). As loss function, we employ a modified form of normalized mean squared error (NMSE):

$$\mathcal{L}_{\text{DL}} = \sum_{i,j} \left(\frac{\mathcal{D}_\Theta(\mathbf{f}^{(i)}, \mathbf{f}^{(j)}) - d_{\text{time},i,j}}{d_{\text{time},i,j} + \beta} \right)^2 \quad (7)$$

In contrast to mean squared error (MSE), NMSE places a higher importance on predicting small time differences correctly by normalizing the error to $d_{\text{time},i,j}$. The additional hyperparameter $\beta > 0$ in Eq. (7) has the following impact on the behavior of \mathcal{L}_{DL} : For $d_{\text{time},i,j} \ll \beta$, Eq. (7) behaves more like the regular MSE loss function, i.e., normalization is applied less aggressively to very small time differences. For $d_{\text{time},i,j} \gg \beta$, Eq. (7) approaches an NMSE loss function, implying that prediction errors for large true time differences $d_{\text{time},i,j}$ are weighted low. Intuitively, this makes sense since we cannot expect \mathcal{D}_Θ to generate accurate distance predictions for large time differences due to unknown UE trajectories.

For training the DNN, we only select pairs of datapoints i, j for which $d_{\text{time},i,j} \leq \alpha$, i.e., for which the absolute time difference is smaller than some threshold α . The DNN \mathcal{D}_Θ consists of four hidden layers with 1024, 512, 256 and 128 neurons each, all of them with ReLU activation. In our experiments, we choose $\beta = 1$ s and $\alpha = 500$ s. Since subsequent processing steps may assume perfectly symmetric dissimilarity matrices, we symmetrize the metric during inference to obtain

$$d_{\text{DL},i,j} = \frac{1}{2} \left(\mathcal{D}_\Theta(\mathbf{f}^{(i)}, \mathbf{f}^{(j)}) + \mathcal{D}_\Theta(\mathbf{f}^{(j)}, \mathbf{f}^{(i)}) \right).$$

G. Fused Dissimilarity Metrics

Observing some pathological situations, illustrated in Fig. 4, leads to the realization that different metrics may fail or perform well under different sets of circumstances: If channel conditions change dramatically over a short spatial distance, as is the case in Fig. 4a, the channel charting algorithm may fail to place neighboring datapoints in proximity to each other in the channel chart if using a CSI-based dissimilarity metric. On the other hand, if a UE takes the Ω -shaped trajectory shown in Fig. 4b, any timestamp-based metric will fail to correctly indicate the closeness of the two turning points.

These two examples, which can occur in real-world datasets, lead us to suggest *fused* dissimilarity metrics that combine information from multiple sources. A fused dissimilarity metric d_{fuse} is computed separately for every combination of two

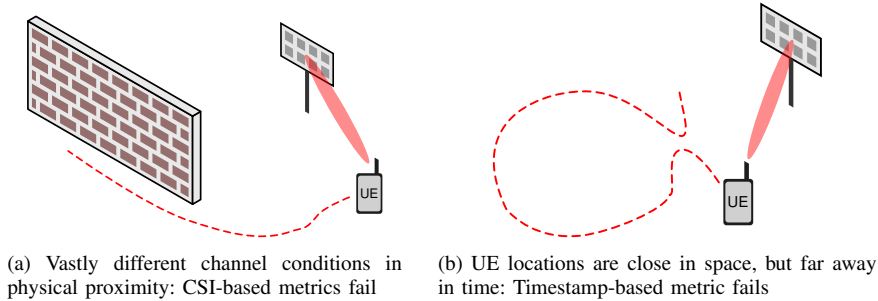


Fig. 4. Pathological cases for CSI- or timestamp-based dissimilarity metrics

datapoints i, j and takes into account two or more other dissimilarity metrics d_A, d_B, \dots :

$$d_{\text{fuse},i,j} = f_{\text{fuse}}(\gamma_A d_{A,i,j}, \gamma_B d_{B,i,j}, \dots) \quad (8)$$

The function f_{fuse} in Eq. (8) defines how the combined metric is calculated. For example, if the dissimilarity metrics are prone to sometimes overestimating the true distance, but immune from underestimating, then f_{fuse} may simply choose the minimum of all metrics. The constants $\gamma_A, \gamma_B, \dots$ in Eq. (8) are scaling factors which may be required to scale all metrics to a common reference. For instance, all metrics may be scaled such that they approximate the true distance in meters. In practice, these scaling factors can often be estimated from the dataset itself. As will be shown in Section VII, the fusion of a CSI-based metric like d_{ADP} with d_{time} as a timestamp-based dissimilarity metric is of particular interest and leads to significant performance improvements.

H. Global Geodesic Dissimilarities

As [16] points out, dissimilarity metrics are most reliable if the true distance between two datapoints is small. On the other hand, if two datapoints are separated widely in physical space, CSI-based dissimilarity metrics are rarely indicative of the true physical distance. A channel chart learned directly from CSI-based dissimilarity metrics without any further processing will usually preserve local neighborhood relationships, but fail at capturing the global topology of the environment. As in [16] and inspired by the idea behind Isomap [23], we compute *geodesic dissimilarities*, which more accurately predict true distances between far-away datapoints. The basic concept is illustrated in Fig. 5: The dissimilarity between two far-away points A and B is computed as the sum of smaller dissimilarities (which are more accurate) between intermediate points that are closer together.

In practice, geodesic distances are computed as follows: First, we find the pairwise dissimilarities between any two datapoints in the dataset using one of the aforementioned metrics and collect them in the dissimilarity matrix $\mathbf{D}_{\text{pw}} \in \mathbb{R}^{L \times L}$. If, as explained in Section III-G, a fused dissimilarity metric shall be used, \mathbf{D}_{pw} must contain the fused dissimilarities. \mathbf{D}_{pw} is interpreted as a matrix containing the weights of a graph, and we find its k -nearest neighbor graph $G_{k\text{-NN}}$, where k is a tunable hyperparameter that we choose as $k = 20$. We then apply a shortest path algorithm, such as Dijkstra's

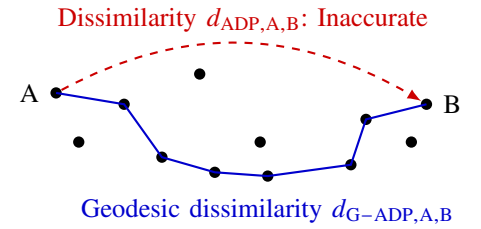


Fig. 5. Illustration of geodesic dissimilarity

algorithm [24] to $G_{k\text{-NN}}$. The length of the computed shortest paths between any two nodes of $G_{k\text{-NN}}$ are the geodesic dissimilarities, which we collect in the geodesic dissimilarity matrix $\mathbf{D}_{\text{geo}} \in \mathbb{R}^{L \times L}$. In our notation, geodesic versions of pairwise dissimilarity metrics are denoted by a "G-" prefix (for example, d_{CIRA} becomes $d_{G\text{-CIRA}}$).

IV. CLASSICAL MANIFOLD LEARNING

Classical manifold learning techniques formulate optimization problems, where the objective is to find a low-dimensional representation, which, according to some cost function, minimizes the discrepancy in point-to-point distances between channel chart and dissimilarity matrix.

A. Multidimensional Scaling and Isomap

Multidimensional scaling (MDS) [25] places points $\{\mathbf{z}^{(l)}\}_{l=1}^L$ in the channel chart such that the mean squared distance between point-to-point distances in the channel chart $\|\mathbf{z}^{(i)} - \mathbf{z}^{(j)}\|_2$ and the dissimilarities $d_{i,j}$ in the dissimilarity matrix is minimized, which is achieved by

$$\min_{\{\mathbf{z}^{(l)}\}_{l=1}^L} \sum_{i=1}^{L-1} \sum_{j=i+1}^L \left(d_{i,j} - \|\mathbf{z}^{(i)} - \mathbf{z}^{(j)}\|_2 \right)^2. \quad (9)$$

This non-convex optimization problem is solved with gradient descent. It is not guaranteed that the global optimum of the objective function is found. Any orthogonal transform of the optimized point set $\{\mathbf{z}^{(l)}\}_{l=1}^L$ is also an optimum. MDS applied to a geodesic dissimilarity matrix is known as Isomap.

B. Sammon's Mapping

SM [10] is a variation of MDS which emphasizes the importance of small point-to-point dissimilarities. This is achieved by adding a weighting factor to the objective function:

$$\min_{\{\mathbf{z}^{(l)}\}_{l=1}^L} \sum_{i=1}^{L-1} \sum_{j=i+1}^L \frac{1}{d_{i,j}} \left(d_{i,j} - \|\mathbf{z}^{(i)} - \mathbf{z}^{(j)}\|_2 \right)^2 \quad (10)$$

C. t -distributed Stochastic Neighbor Embedding

t -distributed stochastic neighbor embedding (t -SNE) [26] is another commonly used manifold learning technique. The algorithm starts by computing what are called conditional probabilities for the distances in the dissimilarity matrix:

$$p_{j|i} = \frac{\exp\left(-d_{i,j}^2/2\sigma_i^2\right)}{\sum_{k \neq i} \exp\left(-d_{i,k}^2/2\sigma_i^2\right)} \quad \text{and} \quad p_{i|i} = 0 \quad (11)$$

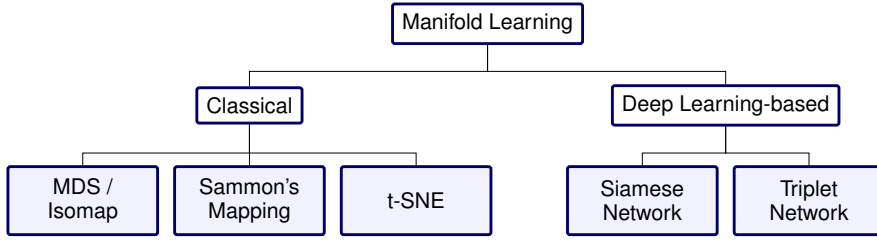


Fig. 6. Overview of classical and deep learning-based manifold learning methods

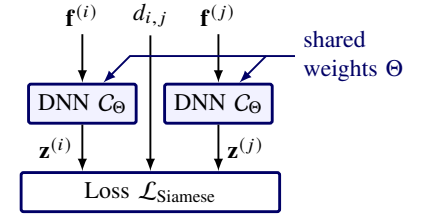


Fig. 7. Siamese neural network structure

In Eq. (11), σ_i is a hyperparameter. For the computation of σ_i , we refer to [26, Section 2] and note that our values of σ_i are based on a “perplexity” of 120, which was empirically found to deliver good results. t-SNE then defines symmetrized conditional probabilities as $p_{ij} = \frac{p_{ji} + p_{ij}}{2L}$ and defines pairwise similarities in the channel chart as

$$q_{ij} = \frac{(1 + \|\mathbf{z}_i - \mathbf{z}_j\|_2^2)^{-1}}{\sum_k \sum_{\ell \neq k} (1 + \|\mathbf{z}_k - \mathbf{z}_\ell\|_2^2)^{-1}} \quad \text{and} \quad q_{ii} = 0.$$

The location of channel chart points $\{\mathbf{z}^{(l)}\}_{l=1}^L$ is then determined by minimizing the Kullback-Leibler divergence:

$$\min_{\{\mathbf{z}^{(l)}\}_{l=1}^L} \sum_{i \neq j} p_{ij} \log \frac{p_{ij}}{q_{ij}}$$

V. DEEP LEARNING-BASED MANIFOLD LEARNING

In the case of deep-learning based manifold learning methods, the FCF is realized as a DNN C_Θ , which maps some CSI feature vector $\mathbf{f}^{(l)}$ (see Section II-C) to the estimated corresponding position in the channel chart $\mathbf{z}^{(l)}$, i.e.,

$$\mathbf{z}^{(l)} = C_\Theta(\mathbf{f}^{(l)}),$$

with Θ being the set of trainable parameters. The challenge is that labels for $\mathbf{z}^{(l)}$ are unavailable, hence C_Θ cannot be trained in a supervised manner. Instead, during the training step, it has been proposed to embed C_Θ into either a *Siamese* [5] or a *triplet* [12] neural network, as explained in the following. For inference, this embedding is no longer required.

A. Siamese Neural Networks

The structure of a Siamese neural network, as illustrated in Fig. 7, enables the use of objective functions known from classical manifold learning techniques as loss function. During training, two weight-sharing DNNs C_Θ map two CSI feature vectors $\mathbf{f}^{(i)}, \mathbf{f}^{(j)}$ to channel chart positions $\mathbf{z}^{(i)}, \mathbf{z}^{(j)}$ at once. Then, the weights are updated based on a loss function $\mathcal{L}_{\text{Siamese}}$ that takes into account $\mathbf{z}^{(i)}, \mathbf{z}^{(j)}$ and the dissimilarity metric $d_{i,j}$ from the dissimilarity matrix. Here, we assume that the MDS cost function is used as loss function for training:

$$\mathcal{L}_{\text{Siamese}} = \sum_{i=1}^{N-1} \sum_{j=i+1}^N (d_{i,j} - \|\mathbf{z}^{(i)} - \mathbf{z}^{(j)}\|_2)^2. \quad (12)$$

As for MDS, this ensures that the DNN learns to place the estimated points such that their distance in the channel chart match with the corresponding computed dissimilarities. In that sense, the Siamese neural network can be seen as a parametric version of MDS. However, other loss functions such as, e.g., Sammon’s loss, could also be used [5].

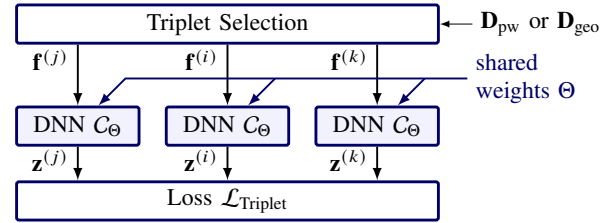


Fig. 8. Triplet neural network structure

B. Triplet Neural Networks

Another approach is to embed the DNN C_Θ into a triplet neural network [27], as depicted in Fig. 8. Here, the loss function does not require information from the dissimilarity matrix. Instead, information about dissimilarities is incorporated into *triplet selection*. This triplet selection step selects 3-tuples $(i, j, k) \in \{1, \dots, L\}^3$ of datapoints, where the datapoint with index i is called the *anchor* sample, datapoint j is the *close* sample and datapoint k is the *far* sample. In our case, we choose the anchor sample i randomly among all datapoints in the dataset with uniform probability. Then, we define the set $\mathcal{N}_q^{(i)}$ of suitable close samples for the anchor sample i as

$$\mathcal{N}_q^{(i)} = \{l \mid d_{i,l} < d_{\text{thresh},q}^{(i)}\},$$

where $d_{\text{thresh},q}^{(i)}$ is the q -quantile of all dissimilarities $\{d_{i,l}\}_{l=1,\dots,L}$. In other words, $\mathcal{N}_q^{(i)}$ contains the qL nearest neighbors of datapoint i with respect to the dissimilarities.

The parameter q is a hyperparameter that may be adjusted during training. We suggest large values for q at first (e.g., $q = 0.2$) and to reduce q over the training epochs (e.g., to $q = 0.02$). This way, the neural network first learns the global and then the local structure of the manifold. Next, the index of the close sample j is picked randomly from $\mathcal{N}_q^{(i)}$, and the index of the far sample k is picked randomly from $\{1, \dots, L\} \setminus \mathcal{N}_q^{(i)}$, in both cases with uniform probability. This process is repeated until the desired number of triplets (i, j, k) has been collected in the set \mathcal{T} . Ideally, each triplet should fulfill

$$\|\mathbf{x}^{(i)} - \mathbf{x}^{(j)}\|_2 < \|\mathbf{x}^{(i)} - \mathbf{x}^{(k)}\|_2 \quad \text{with} \quad (i, j, k) \in \mathcal{T}. \quad (13)$$

That is, in physical space, the close sample should be nearer to the anchor sample than the far sample. Since triplet selection guarantees that $d_{i,j} < d_{i,k}$, Eq. (13) should be fulfilled for most triplets as long as a good dissimilarity metric is chosen.

The three weight-sharing DNNs estimate channel chart positions $\mathbf{z}^{(i)}, \mathbf{z}^{(j)}$ and $\mathbf{z}^{(k)}$ based on the CSI feature vectors

$\mathbf{f}^{(i)}$, $\mathbf{f}^{(j)}$ and $\mathbf{f}^{(k)}$. The triplet loss $\mathcal{L}_{\text{Triplet}}$ [27] then makes use of the knowledge that $\mathbf{z}^{(j)}$ should be closer to $\mathbf{z}^{(i)}$ than $\mathbf{z}^{(k)}$:

$$\mathcal{L}_{\text{Triplet}} = \sum_{(i,j,k) \in \mathcal{T}} \frac{\max \{ \|\mathbf{z}^{(i)} - \mathbf{z}^{(j)}\|_2 - \|\mathbf{z}^{(i)} - \mathbf{z}^{(k)}\|_2 + M, 0 \}}{|\mathcal{T}|}, \quad (14)$$

In Eq. (14), M is yet another hyperparameter called *margin* that we choose to be $M = 1$. In contrast to Siamese networks, triplet neural networks only require qualitative information about dissimilarities: It is sufficient to know that the close sample is closer to the anchor than the far sample. Therefore, triplet neural networks only require a monotonically positive relationship between true distances $\|\mathbf{x}^{(i)} - \mathbf{x}^{(j)}\|_2$ and dissimilarities $d_{i,j}$, but not necessarily the proportional relationship stipulated in Eq. (2). This is a key advantage for metrics that do not approximate the proportional relationship (e.g., d_{time}), but can also be a disadvantage if good absolute dissimilarities are available, but the information is not used.

VI. EVALUATION METRICS

The quality of a channel chart can be subjectively judged by comparing the learned chart to the map of true locations. However, for a more objective assessment, well-known evaluation metrics from manifold learning like continuity (CT), trustworthiness (TW) [28] and Kruskal's stress (KS) [25] are commonly applied. While CT and TW indicate how well local neighborhood relationships are reflected in the channel chart, KS measures to what extent the global structure is preserved.

Instead of applying these metrics to the resulting channel chart, and thereby evaluating dissimilarity metric and manifold learning technique jointly, CT, TW and KS may also be used to evaluate dissimilarity metrics separately [4]. We also consider Rajski's distance (RD) [29] for dissimilarity metrics and, for channel charts, we compute the mean absolute error (MAE) between the ground truth positions and the channel chart positions assuming an optimal affine coordinate transform.

A. Continuity and Trustworthiness

CT and TW compare neighborhood relationships in physical space to neighborhood relationships in the representation space. Let $r_{l,i}$ denote the rank of the neighbor with index i among all neighbors of datapoint l in physical space. That is, $r_{l,i} = 1$ if i is the closest neighbor of l , $r_{l,i} = 2$ if it is the second closest neighbor and so on. We define the set of K nearest neighbors of l in physical space as $\mathcal{V}_K^{(l)} = \{i \mid r_{l,i} \leq K\}$.

In a similar way, let $\hat{r}_{l,i}$ denote the rank of the neighbor with index i among all neighbors of datapoint l in the representation space. When evaluating CT / TW of a dissimilarity metric, this rank is calculated over the entries in the dissimilarity matrix, i.e., over $\{d_{l,i}\}_{i=1,\dots,L}$. If CT / TW are applied to a channel chart, the rank is calculated over the Euclidean distances of the channel chart locations, i.e., over $\{\|\mathbf{z}^{(l)} - \mathbf{z}^{(i)}\|_2\}_{i=1,\dots,L}$. We define the set of K nearest neighbors of l in the representation space as $\mathcal{U}_K^{(l)} = \{i \mid \hat{r}_{l,i} \leq K\}$. CT is then defined as

$$\text{CT}(K) = 1 - \frac{2}{LK(2L-3K-1)} \sum_{l=1}^L \sum_{i \in \mathcal{V}_K^{(l)}} \max \{0, \hat{r}_{l,i} - K\},$$

and, intuitively speaking, indicates whether the nearest neighbors in physical space are among those of the representation space. Analogously, TW is defined as

$$\text{TW}(K) = 1 - \frac{2}{LK(2L-3K-1)} \sum_{l=1}^L \sum_{i \in \mathcal{U}_K^{(l)}} \max \{0, r_{l,i} - K\},$$

and indicates whether the neighbors in representation space are among those in physical space, or, conversely, if the representation contains false neighbors. The normalization factor ensures that both CT and TW are in the range $[0, 1]$, where values close to 1 are better. As already proposed in [4], we choose a neighborhood size of $K = 0.05L$.

B. Kruskal's Stress

KS [25] is a performance measure for the preservation of the global structure of the channel chart. It compares pairwise distances between points in the original space to those between points in the representation space:

$$\text{KS} = \sqrt{\frac{\sum_{i=1}^{L-1} \sum_{j=i+1}^L (\|\mathbf{x}^{(i)} - \mathbf{x}^{(j)}\|_2 - \beta \|\mathbf{z}^{(i)} - \mathbf{z}^{(j)}\|_2)^2}{\sum_{i=1}^{L-1} \sum_{j=i+1}^L \|\mathbf{x}^{(i)} - \mathbf{x}^{(j)}\|_2^2}}$$

with $\beta = \frac{\sum_{i=1}^{L-1} \sum_{j=i+1}^L \|\mathbf{x}^{(i)} - \mathbf{x}^{(j)}\|_2 \|\mathbf{z}^{(i)} - \mathbf{z}^{(j)}\|_2}{\sum_{i=1}^{L-1} \sum_{j=i+1}^L \|\mathbf{z}^{(i)} - \mathbf{z}^{(j)}\|_2^2}$.

The scaling factor β ensures that the value of KS is bounded to the range $[0, 1]$, where 0 indicates the best preservation of the global structure. If KS is evaluated for a dissimilarity metric (as opposed to a channel chart), $\|\mathbf{z}^{(i)} - \mathbf{z}^{(j)}\|_2$ is replaced by the corresponding dissimilarity $d_{i,j}$.

C. Rajski's Distance

RD, which was proposed for use in channel charting in [22], is an indicator for the mutual information between the true distances and the dissimilarities. To this end, all pairwise true distances $\|\mathbf{x}^{(l)} - \mathbf{x}^{(i)}\|_2$, as well as all dissimilarities $d_{l,i}$ ($l, i \in \{1, \dots, L\}$) are quantized into 100 bins each such that they can be interpreted as distributions modeled by the random variables V and Q , respectively. RD is then defined as [29]

$$\text{RD}(V, Q) = 1 - \frac{I(V, Q)}{H(V, Q)}, \quad \text{for } H(V, Q) \neq 0,$$

$$\text{with } I(V, Q) = \sum_{v \in V, q \in Q} P_{V, Q}(v, q) \log_2 \frac{P_{V, Q}(v, q)}{P_V(v) P_Q(q)}$$

denoting the mutual information between the distributions of V and Q , where $P_{V, Q}(v, q)$ is the joint probability distribution of V and Q and $P_V(v)$ and $P_Q(q)$ are the respective marginal distributions. The joint entropy of V and Q is given by

$$H(V, Q) = - \sum_{v \in V, q \in Q} P_{V, Q}(v, q) \log_2 P_{V, Q}(v, q).$$

RD is between 0 and 1, and 0 indicates the best performance.

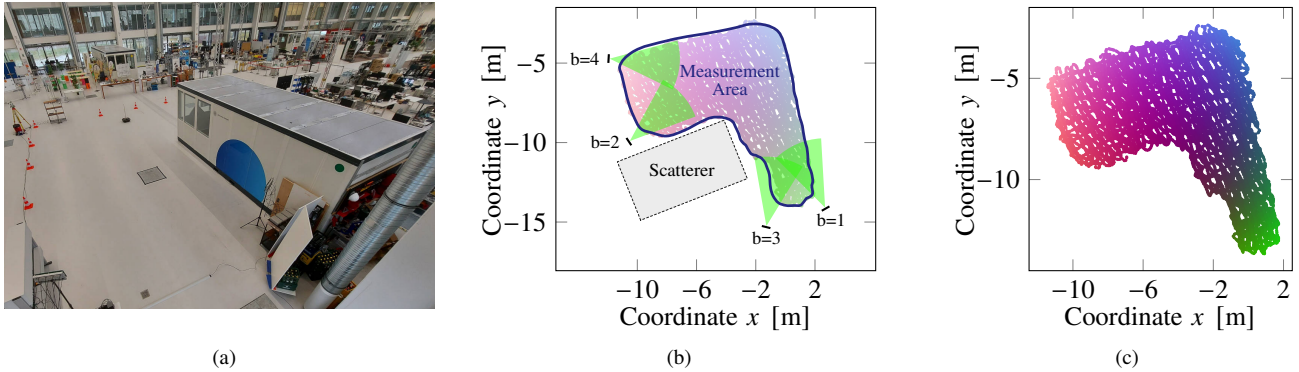


Fig. 9. Information about the industrial environment the measurement was conducted in. The figure shows (a) a photograph of the environment, (b) a top view map and (c) a scatter plot of colored “ground truth” positions of datapoints in $\mathcal{S}_{\text{full}}$, also in top view. The antenna arrays in the map are drawn to scale as black rectangles and their viewing direction is indicated by the green sectors.

D. Mean Absolute Error

A learned channel chart should reconstruct both local and global geometry, but may be rotated, scaled, flipped and / or translated compared to the true map. As previously proposed by Stahlke et al. [16], we find the optimal affine transformation from channel chart to the true locations and compute the MAE under the assumption that this transformation has been found and applied. The resulting MAE thereby provides a lower bound to the absolute localization error. We anticipate that it will be possible to achieve performance close to this bound by applying proposals like [21]. To find the optimal affine transformation, we solve the least squares problem

$$(\hat{\mathbf{A}}, \hat{\mathbf{b}}) = \arg \min_{(\mathbf{A}, \mathbf{b})} \sum_{l=1}^L \|\mathbf{A}\mathbf{z}^{(l)} + \mathbf{b} - \mathbf{x}^{(l)}\|_2^2$$

and compute the MAE as $\text{MAE} = \frac{1}{L} \sum_{l=1}^L \|\hat{\mathbf{A}}\mathbf{z}^{(l)} + \hat{\mathbf{b}} - \mathbf{x}^{(l)}\|_2$.

VII. EXPERIMENTAL RESULTS

A. DICHASUS: Channel Measurement Datasets

All dissimilarity metrics and manifold learning techniques were tested on a dataset generated by *Distributed Channel Sounder by University of Stuttgart (DICHASUS)*, our distributed mMIMO channel sounder, whose architecture is thoroughly described in [30]. In brief, DICHASUS measures the propagation channel between a single transmitter and many receive antennas. It achieves long-term phase-coherence, even if antennas are distributed over a wide area. DICHASUS provides large datasets containing frequency-domain CSI tensors $\mathbf{H}^{(l)}$, alongside side information like timestamps and accurate information about the positions of all antennas.

The dataset chosen for the following analyses is called *dichasus-cf0x* [31], and was captured in an industrial environment with $B = 4$ separate antenna arrays made up of $M = 2 \times 4$ antennas each. $N_{\text{sub}} = 1024$ OFDM channel coefficients were measured at a carrier frequency of 1.272 GHz and with a channel bandwidth of 50 MHz. The single dipole transmit antenna is mounted on top of a robot, which travels along a set of trajectories inside a defined, L-shaped area, with an overall size of approximately $14 \text{ m} \times 14 \text{ m}$. A photo and a top view map of the environment are shown in Fig. 9. A large

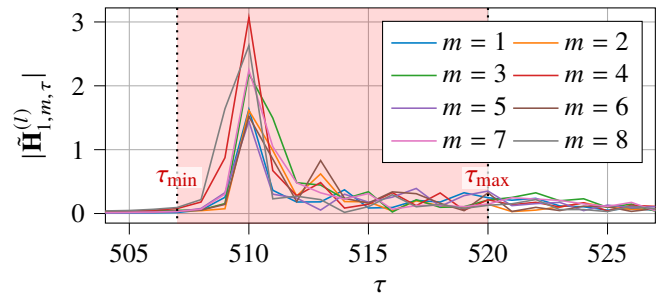


Fig. 10. Exemplary time-domain CSI amplitudes $|\tilde{\mathbf{H}}_{l,m,\tau}^{(l)}|$ at some time instant l . Each line corresponds to one antenna m at antenna array $b = 1$.

metal container is located at the inner corner of the L-shape, blocking the LoS. Every position in the measurement area has at least one LoS path to one of the four arrays, and some positions in the dataset even have a LoS path to all arrays.

To reduce the total amount of data, we choose three subsets of *dichasus-cf0x* called *dichasus-cf02*, *dichasus-cf03* and *dichasus-cf04* and then collect only every 5th datapoint into a smaller dataset that we call $\mathcal{S}_{\text{full}}$, now containing $|\mathcal{S}_{\text{full}}| = 16797$ datapoints. The true datapoint positions $\mathbf{x}^{(l)}$ are shown in Fig. 9. The points have been colorized and the datapoints will retain their color even as the FCF maps them to a position in the channel chart. This allows for a visual evaluation of the generated chart: If the global topology is preserved, a similar color gradient should appear in the chart.

Exemplary CSI data measured by DICHASUS is visualized in Fig. 10, which shows the CIRs of all antennas in antenna array $b = 1$. Note that phase information is also available, but not displayed in the figure. It is easy to see that much of the received signal power is concentrated within a relatively short interval of taps (area shaded red in Fig. 10), leading us to choose $\tau_{\text{min}} = 507$ and $\tau_{\text{max}} = 520$ for all subsequent analyses.

B. Fusion of d_{ADP} and d_{time}

As described in Section III-G, multiple dissimilarity metrics may be combined into a fused metric. We choose to fuse d_{ADP} as a CSI-based dissimilarity metric and d_{time} as a side information-based metric and show that using the fused metric d_{fuse} significantly improves the channel chart. In *dichasus-*

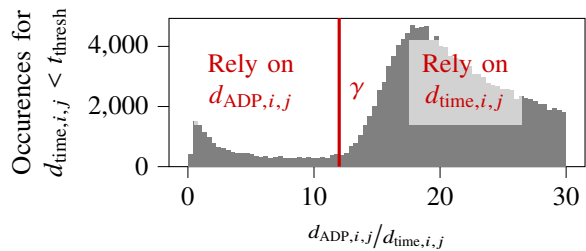


Fig. 11. Histogram depicting the distribution of the ratios $d_{ADP,i,j}/d_{time,i,j}$ for over all pairs of datapoints i, j in \mathcal{S}_{full} with $d_{time,i,j} < t_{thresh}$.

cf0x, the robot either moves at approximately constant velocity v_{robot} , or remains at a standstill. The combination of d_{ADP} and d_{time} is based on a simple assumption: For short time intervals $d_{time} < t_{thresh}$, we assume that the transmitter either moves along an approximately straight line (due to its inertia) with velocity v_{robot} or does not move at all. For such short intervals, if the robot is moving, the time-based metric d_{time} predicts the true distance between points much better than any CSI-based metric could. Therefore, we propose to fuse d_{time} and d_{ADP} by taking their minimum after appropriate scaling of d_{time} :

$$d_{fuse,i,j} = \min \{d_{ADP,i,j}, \gamma \cdot d_{time,i,j}\} \quad (15)$$

This way, whenever $d_{time,i,j}$ is sufficiently small, it predicts the dissimilarity between points i and j . The challenge remains to find the scaling factor γ in Eq. (15): To determine γ , we need to observe the distribution of ratios $d_{ADP,i,j}/d_{time,i,j}$ in Fig. 11, there shown for all pairs of datapoints i, j in \mathcal{S}_{full} with $d_{time,i,j} < t_{thresh} = 2$ s. The diagram clearly shows a bimodal distribution for the ratios, where the right mode can be attributed to the datapoints where the robot is moving, and the left mode can be attributed to the cases where it remains static. We choose a scaling factor that separates the two modes, e.g., $\gamma = 12$, such that $\gamma d_{time,i,j} < d_{ADP,i,j}$ if the robot is moving. For other real-world datasets, the assumption of constant transmitter velocity may not hold. In that case, it might be necessary to estimate the relative velocities of transmitters over time and between transmitters based on CSI data. This remains a topic for future research that we do not consider within the scope of this work. After computing the pairwise fused metric $d_{fuse,i,j}$, we find geodesic distances as explained in Section III-H to obtain $d_{G-fuse,i,j}$.

C. Evaluation of Dissimilarity Metrics

In Tab. I, all dissimilarity metrics presented in Section III, as well as previously described fused dissimilarity metric $d_{fuse,i,j}$ are evaluated using CT, TW, KS and RD. The true distance $d_{Euc,i,j}$ is only included for reference and it obviously achieves the optimal performance metric in every category. In all tables, results based on true distances are only included for comparison and are shaded in grey. The results indicate that our newly proposed dissimilarity metrics d_{ADP} and d_{DL} outperform the baseline dissimilarities d_{CS} and d_{CIRA} regarding most performance metrics. Overall, the geodesic fused dissimilarity $d_{G-fuse,i,j}$ is the best-performing one.

In general, it is apparent that geodesic dissimilarities are better than the respective non-geodesic versions regarding CT,

TABLE I
EVALUATION OF DISSIMILARITY METRICS ON \mathcal{S}_{full} .

Dissimilarity	CT \uparrow	TW \uparrow	KS \downarrow	RD \downarrow
d_{Euc}	1.0000	1.0000	0.0000	0.0000
d_{G-Euc}	0.9999	1.0000	0.0231	0.3617
d_{CS}	0.9529	0.9542	0.4281	0.9595
d_{G-CS}	0.9799	0.9774	0.2676	0.9112
d_{CIRA}	0.9278	0.9477	0.3173	0.9406
d_{G-CIRA}	0.9685	0.9684	0.2197	0.8972
d_{DL}	0.9762	0.9742	0.4267	0.9499
d_{G-DL}	0.9800	0.9772	0.2250	0.8953
d_{ADP}	0.9653	0.9689	0.4350	0.9431
d_{G-ADP}	0.9885	0.9866	0.1738	0.8384
d_{fuse}	0.9655	0.9691	0.4347	0.9429
d_{G-fuse}	0.9957	0.9948	0.1098	0.7619

TW, KS and RD. This is also illustrated by Fig. 12, which, inspired by [16], plots $d_{ADP,i,j}$ and $d_{G-ADP,i,j}$ as a function of the Euclidean distance $d_{Euc,i,j}$. Unsurprisingly, the geodesic dissimilarity approximates the Euclidean distance better (down to a scaling factor) than the non-geodesic dissimilarity.

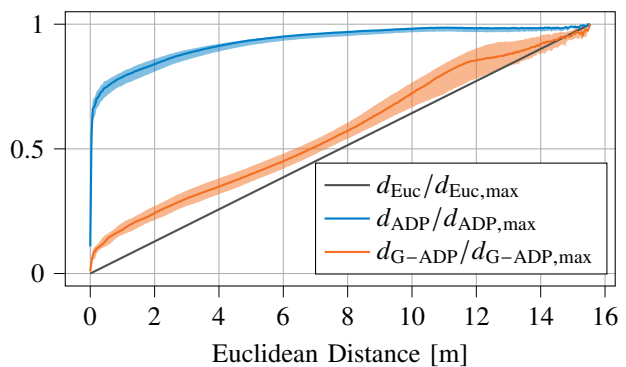


Fig. 12. Dissimilarity metrics d_{ADP} and d_{G-ADP} normalized to a range from 0 to 1 as a function of the true distance. To generate the diagram, the dissimilarities are grouped into 100 bins according to the true distances. The lines represent the medians of these bins, and the shaded areas represent the range from the 25th to the 75th percentile. See also [16, Fig. 6 and 7].

D. Channel Charting Results

All channel charts in this section are learned on the training set \mathcal{S}_{full} , as specified in Section VII-A. While classical manifold learning methods directly produce channel charts, deep learning-based (parametric) methods are evaluated on a different test set \mathcal{S}'_{full} . This test set also contains $|\mathcal{S}'_{full}| = 16797$ datapoints measured in the same area, and is generated by selecting a different subset of points from *dichasus-cf02*, *dichasus-cf03* and *dichasus-cf04*. This ensures that deep learning-based methods actually work with previously unseen feature vectors, and, in a performance comparison, puts them at a slight disadvantage compared to classical methods.

In our experiments, the DNN \mathcal{C}_{Θ} consists of six hidden layers with 1024, 512, 512, 256, 128, 64 neurons and ReLU activation each, and an output layer with 2 neurons and linear activation. Batch normalization is applied between the layers to enhance training performance.

Tab. II shows the channel charting performance for different classical methods. The results for the distance d_{Euc} serve as benchmark for the respective manifold learning technique. As expected, the channel charts learned by SM often represent the local geometry better than those learned by MDS (higher CT / TW). Overall, the best performance is achieved by Isomap, which applies MDS to geodesic distances. As already concluded in Section VII-C, the newly introduced dissimilarity metrics, and especially the fused metric appear to be most suitable, as they result in the best channel charts. It is remarkable that the t-SNE algorithm produces only slightly worse channel charts than Isomap without relying on geodesic distances.

The performance metrics for deep learning-based methods are shown in Tab. III. Unsurprisingly, the Siamese network produces better channel charts for most geodesic dissimilarity metrics, whereas the triplet neural network performs better for non-geodesic metrics. This can be explained by the fact that the triplet neural network only uses qualitative information about dissimilarity, and does not require the metrics to be proportional to true distances, whereas the Siamese network can also make use of absolute dissimilarity information.

The channel chart produced by a triplet neural network using purely time-based triplet selection (d_{time}) is surprisingly good with respect to all metrics, but is still outperformed by the Siamese network: The best overall performance is achieved by the Siamese network in combination with $d_{\text{G-fuse}}$.

After the optimal affine coordinate transformation has been applied as in Section VI-D, the cumulative distribution function (CDF) of the absolute localization errors can be visualized. Various such CDFs, belonging to channel charts produced with different dissimilarities and manifold learning techniques, are depicted in Fig. 13. Fig. 14 shows several channel charts obtained using different dissimilarity metrics and manifold learning techniques. The channel charts can be directly compared to the true map in Fig. 9c. The first row of Fig. 14 shows the channel charts produced with the baseline metrics $d_{\text{G-CIRA}}$ and $d_{\text{G-CS}}$ as well as a chart learned from non-geodesic d_{ADP} by Siamese network. It also contains Fig. 14d, which is the surprisingly good channel chart obtained through time-based triplet selection, i.e., the combination of a triplet network with d_{time} . The second row shows channel charts for $d_{\text{G-ADP}}$, demonstrating that using the geodesic version of the ADP metric greatly improves performance. What is more, the fused metric $d_{\text{G-fuse}}$, here with Isomap or a Siamese network, generates even better channel charts.

E. Results for significant NLoS propagation

To figure out whether our metrics $d_{\text{G-DL}}$, $d_{\text{G-ADP}}$ and $d_{\text{G-fuse}}$ are useful for environments with significant NLoS propagation, we define a dataset $\mathcal{S}_{\text{NLoS}}$, which we obtain by removing CSI data for antenna arrays $b = 2$ and $b = 4$ from $\mathcal{S}_{\text{full}}$. This way, the metal container is blocking the LoS path for a significant share of the area (compare Fig. 9b). Tab. IV shows the performance of the respective dissimilarities for this scenario. All metrics perform at least slightly worse than in the LoS scenario (compare Tab. I), but the CSI-based dissimilarity metrics suffer most from the NLoS conditions. d_{CS} and

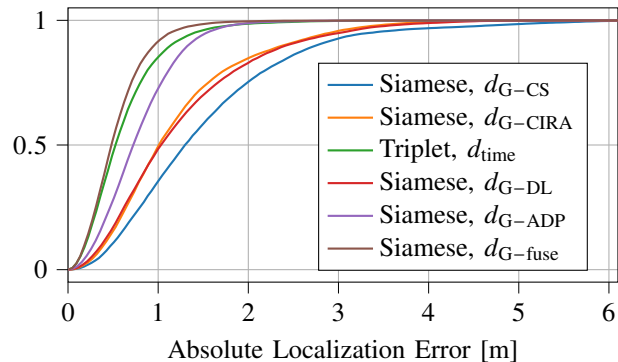


Fig. 13. CDF of absolute localization error for different manifold learning methods and dissimilarity metrics, computed on $\mathcal{S}_{\text{full}}$.

TABLE II
PERFORMANCE OF CLASSICAL METHODS ON $\mathcal{S}_{\text{full}}$.

Method	Metric	CT \uparrow	TW \uparrow	KS \downarrow	MAE \downarrow	Fig.
MDS	d_{Euc}	1.0000	1.0000	0.0001	0.000 m	
MDS	d_{CS}	0.9106	0.8888	0.3673	1.913 m	
MDS	d_{CIRA}	0.9281	0.9200	0.3400	1.861 m	
MDS	d_{DL}	0.9289	0.9011	0.4015	2.349 m	
MDS	d_{ADP}	0.8902	0.9007	0.3437	2.037 m	
MDS	d_{fuse}	0.9254	0.9255	0.3262	1.782 m	
Isomap	$d_{\text{G-CS}}$	0.9712	0.9721	0.2557	1.533 m	
Isomap	$d_{\text{G-CIRA}}$	0.9690	0.9656	0.2340	1.185 m	
Isomap	$d_{\text{G-DL}}$	0.9689	0.9617	0.2237	1.292 m	
Isomap	$d_{\text{G-ADP}}$	0.9893	0.9878	0.1371	0.705 m	
Isomap	$d_{\text{G-fuse}}$	0.9956	0.9960	0.0859	0.438 m	14g
SM	d_{Euc}	0.9833	0.9339	0.1853	1.274 m	
SM	d_{CS}	0.9311	0.8984	0.3482	1.877 m	
SM	d_{CIRA}	0.9124	0.9167	0.3242	1.787 m	
SM	d_{DL}	0.9231	0.8572	0.4249	2.454 m	
SM	d_{ADP}	0.9493	0.9383	0.3159	1.518 m	
SM	d_{fuse}	0.9529	0.9413	0.3153	1.505 m	
t-SNE	d_{Euc}	0.9980	0.9969	0.1025	0.894 m	
t-SNE	d_{CS}	0.9811	0.9819	0.1800	1.030 m	
t-SNE	d_{CIRA}	0.9579	0.9514	0.2392	1.261 m	
t-SNE	d_{DL}	0.9793	0.9778	0.1637	0.914 m	
t-SNE	d_{ADP}	0.9851	0.9874	0.1776	0.775 m	
t-SNE	d_{fuse}	0.9888	0.9902	0.1509	0.697 m	

d_{CIRA} are especially hard hit, but the performance metrics for d_{ADP} also deteriorate. Fusing d_{ADP} with d_{time} and using geodesic dissimilarities significantly improves performance, as indicated by the analyses for $d_{\text{G-fuse}}$. This underlines the importance of taking into account timestamp information, especially in NLoS conditions. The results for Isomap, Siamese networks and triplet networks on the NLoS dataset are listed in Tab. V. As expected, the channel charts produced with metrics that exploit timestamp information perform best.

This claim is supported by the final row of Fig. 14: The global geometry is distorted for the channel chart produced with $d_{\text{G-ADP}}$, whereas the channel charts using timestamp-aided dissimilarity metrics ($d_{\text{G-DL}}$, d_{time} and $d_{\text{G-fuse}}$) are globally more meaningful. The best localization performance is achieved by the Siamese network combined with the fused dissimilarity $d_{\text{G-fuse}}$, where a mean localization error of 0.672 m is reached. As before, CDFs of localization errors for different metrics and techniques are shown in Fig. 15.

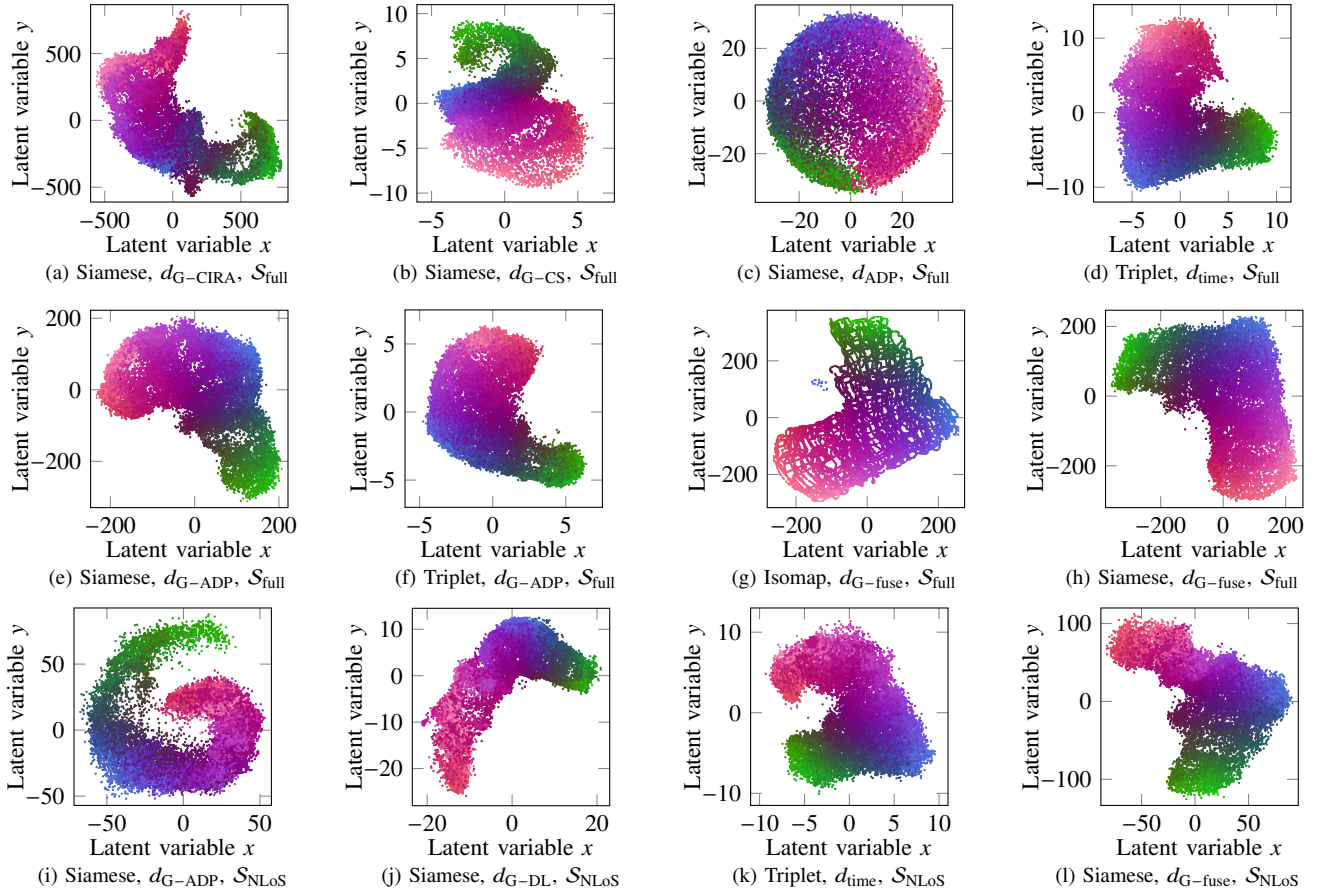


Fig. 14. Comparison of channel charts generated by various combinations of manifold learning technique, dissimilarity metric and dataset (see captions).

TABLE III
PERFORMANCE OF DEEP LEARNING-BASED METHODS ON S_{full}

Method	Metric	CT \uparrow	TW \uparrow	KS \downarrow	MAE \downarrow	Fig.
Siamese	d_{Euc}	0.9907	0.9902	0.0801	0.364 m	
Siamese	d_{CS}	0.8928	0.8869	0.3394	1.712 m	
Siamese	d_{CIRA}	0.9195	0.9040	0.3344	1.926 m	
Siamese	d_{DL}	0.8982	0.8681	0.4020	2.368 m	
Siamese	d_{ADP}	0.8882	0.8845	0.3496	1.817 m	14c
Siamese	d_{fuse}	0.8907	0.8845	0.3466	1.771 m	
Siamese	$d_{\text{G-CS}}$	0.9710	0.9718	0.2517	1.519 m	14b
Siamese	$d_{\text{G-CIRA}}$	0.9524	0.9466	0.2266	1.216 m	14a
Siamese	$d_{\text{G-DL}}$	0.9638	0.9530	0.2269	1.250 m	
Siamese	$d_{\text{G-ADP}}$	0.9807	0.9798	0.1515	0.783 m	14e
Siamese	$d_{\text{G-fuse}}$	0.9879	0.9880	0.1067	0.542 m	14h
Triplet	d_{Euc}	0.9825	0.9803	0.1338	0.671 m	
Triplet	d_{CS}	0.9470	0.9362	0.3011	1.675 m	
Triplet	d_{CIRA}	0.9299	0.9265	0.2770	1.429 m	
Triplet	d_{DL}	0.9487	0.9246	0.3198	2.178 m	
Triplet	d_{ADP}	0.9656	0.9594	0.2810	1.420 m	
Triplet	d_{fuse}	0.9657	0.9601	0.2781	1.438 m	
Triplet	d_{time}	0.9823	0.9822	0.2155	0.621 m	14d
Triplet	$d_{\text{G-CS}}$	0.9702	0.9669	0.1733	0.951 m	
Triplet	$d_{\text{G-CIRA}}$	0.9533	0.9430	0.2215	1.239 m	
Triplet	$d_{\text{G-DL}}$	0.9640	0.9538	0.2241	1.199 m	
Triplet	$d_{\text{G-ADP}}$	0.9769	0.9743	0.1506	0.747 m	14f
Triplet	$d_{\text{G-fuse}}$	0.9805	0.9785	0.1429	0.640 m	

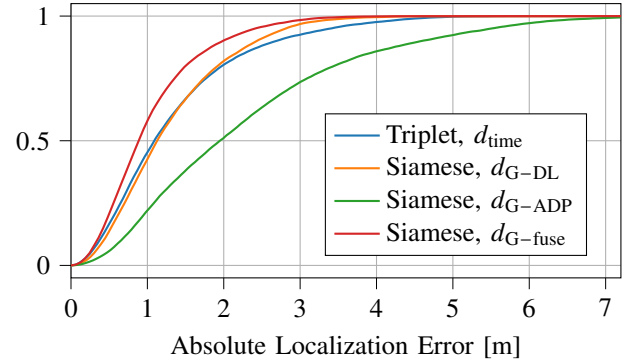


Fig. 15. CDF of absolute localization error for different dissimilarity metrics and manifold learning techniques computed on S_{NLoS} .

VIII. CONCLUSION

With our ADP-based metric, dissimilarity learning and the concept of fused metrics, we propose three novel metrics for channel charting. An extensive study on a publicly available dataset demonstrates that we are capable of reconstructing the global geometry of the environment, outperforming previously proposed metrics. Using our fused metric and a Siamese neural network, we achieve a mean absolute localization error of 0.542 m on the whole dataset when assuming an ideal coordinate transformation from channel chart to spatial coordinates. With a mean absolute error of 1.042 m, performance is

TABLE IV
EVALUATION OF DISSIMILARITY METRICS ON S_{NLoS}

Distance	CT \uparrow	TW \uparrow	KS \downarrow	RD \downarrow
d_{CS}	0.8362	0.8221	0.4338	0.9781
d_{G-CS}	0.8285	0.8141	0.4349	0.9752
d_{CIRA}	0.7599	0.8546	0.4174	0.9691
d_{G-CIRA}	0.6025	0.6066	0.4693	0.9869
d_{DL}	0.9649	0.9497	0.4450	0.9611
d_{G-DL}	0.9679	0.9508	0.3210	0.9295
d_{ADP}	0.9072	0.9027	0.4297	0.9671
d_{G-ADP}	0.9516	0.9299	0.3521	0.9490
d_{fuse}	0.9081	0.9038	0.4294	0.9668
d_{G-fuse}	0.9823	0.9699	0.2204	0.8889

TABLE V
CHANNEL CHARTING PERFORMANCE ON S_{NLoS} .

Method	Metric	CT \uparrow	TW \uparrow	KS \downarrow	MAE \downarrow	Fig.
Isomap	d_{G-DL}	0.9623	0.9485	0.3300	1.955 m	
Isomap	d_{G-ADP}	0.9387	0.8904	0.3759	2.298 m	
Isomap	d_{G-fuse}	0.9778	0.9664	0.2041	0.935 m	
Siamese	d_{Euc}	0.9866	0.9855	0.0961	0.419 m	
Siamese	d_{G-DL}	0.9581	0.9420	0.3233	1.297 m	14j
Siamese	d_{G-ADP}	0.9352	0.8864	0.3760	2.291 m	14i
Siamese	d_{G-fuse}	0.9656	0.9512	0.2150	1.042 m	14l
Triplet	d_{Euc}	0.9769	0.9728	0.1486	0.701 m	
Triplet	d_{G-DL}	0.9591	0.9391	0.2743	1.867 m	
Triplet	d_{G-ADP}	0.9477	0.9162	0.3894	2.292 m	
Triplet	d_{G-fuse}	0.9633	0.9423	0.2768	1.323 m	
Triplet	d_{time}	0.9704	0.9576	0.2795	1.341 m	14k

acceptable even for the NLoS dataset with two missing antenna arrays. Improving methods to find the ideal transformation from channel chart to spatial coordinates, enabling absolute localization, is one potential topic for future research. This work highlights the significance of the dissimilarity metric, illustrating that the quality of dissimilarities is at least as, if not more impactful than the applied manifold learning technique. We encourage others to experiment on our publicly available dataset and to propose even better metrics or techniques.

REFERENCES

- [1] V. Savic and E. G. Larsson, "Fingerprinting-based positioning in distributed massive MIMO systems," in *2015 IEEE 82nd vehicular technology conference (VTC2015-Fall)*. IEEE, 2015.
- [2] J. Vieira, E. Leitinger, M. Sarajlic, X. Li, and F. Tufvesson, "Deep convolutional neural networks for massive MIMO fingerprint-based positioning," in *2017 IEEE 28th Annual International Symposium on Personal, Indoor, and Mobile Radio Communications (PIMRC)*, 2017.
- [3] P. Ferrand, A. Decurninge, and M. Guillaud, "DNN-based Localization from Channel Estimates: Feature Design and Experimental Results," *CoRR*, vol. abs/2004.00363, 2020.
- [4] C. Studer, S. Medjkouh, E. Gönültaş, T. Goldstein, and O. Tirkkonen, "Channel Charting: Locating Users within the Radio Environment using Channel State Information," *CoRR*, vol. abs/1807.05247, 2018.
- [5] E. Lei, O. Castañeda, O. Tirkkonen, T. Goldstein, and C. Studer, "Siamese Neural Networks for Wireless Positioning and Channel Charting," in *57th Annual Allerton Conference on Communication, Control, and Computing*, 2019.
- [6] P. Agostini, Z. Utkovski, S. Stańczak, A. A. Memon, B. Zafar, and M. Haardt, "Not-too-deep channel charting (n2d-cc)," in *2022 IEEE Wireless Communications and Networking Conference (WCNC)*, 2022.
- [7] P. Kazemi, H. Al-Tous, C. Studer, and O. Tirkkonen, "SNR Prediction in Cellular Systems based on Channel Charting," in *2020 IEEE Eighth International Conference on Communications and Networking (ComNet)*.
- [8] —, "Channel charting assisted beam tracking," in *2022 IEEE 95th Vehicular Technology Conference: (VTC2022-Spring)*, 2022.
- [9] H. Hotelling, "Analysis of a complex of statistical variables into principal components," *Journal of Educational Psychology*, vol. 24, no. 6, 1933.
- [10] J. Sammon, "A nonlinear mapping for data structure analysis," *IEEE Transactions on Computers*, vol. C-18, no. 5, pp. 401–409, 1969.
- [11] P. Huang, O. Castañeda, E. Gönültaş, S. Medjkouh, O. Tirkkonen, T. Goldstein, and C. Studer, "Improving channel charting with representation-constrained autoencoders," in *2019 IEEE 20th International Workshop on Signal Processing Advances in Wireless Communications (SPAWC)*. IEEE, 2019, pp. 1–5.
- [12] P. Ferrand, A. Decurninge, L. G. Ordoñez, and M. Guillaud, "Triplet-Based Wireless Channel Charting: Architecture and Experiments," *IEEE Journal on Selected Areas in Communications*, vol. 39, no. 8, 2021.
- [13] J. Deng, S. Medjkouh, N. Malm, O. Tirkkonen, and C. Studer, "Multi-point Channel Charting for Wireless Networks," in *2018 52nd Asilomar Conference on Signals, Systems, and Computers*, 2018, pp. 286–290.
- [14] P. Agostini, Z. Utkovski, and S. Stańczak, "Channel Charting: an Euclidean Distance Matrix Completion Perspective," in *ICASSP 2020 - 2020 IEEE International Conference on Acoustics, Speech and Signal Processing (ICASSP)*, 2020, pp. 5010–5014.
- [15] L. Le Magoarou, "Efficient channel charting via phase-insensitive distance computation," 2021.
- [16] M. Stahlke, G. Yammine, T. Feigl, B. M. Eskofier, and C. Mutschler, "Indoor localization with robust global channel charting: A time-distance-based approach," *IEEE Transactions on Machine Learning in Communications and Networking*, pp. 1–1, 2023.
- [17] H. Al-Tous, P. Kazemi, C. Studer, and O. Tirkkonen, "Channel Charting with Angle-Delay-Power-Profile Features and Earth-Mover Distance," in *2022 56th Asilomar Conference on Signals, Systems, and Computers*, 2022, pp. 1195–1201.
- [18] F. Euchner, P. Stephan, M. Gauger, S. Dörner, and S. Ten Brink, "Improving Triplet-Based Channel Charting on Distributed Massive MIMO Measurements," in *2022 IEEE 23rd International Workshop on Signal Processing Advances in Wireless Communication (SPAWC)*, 2022.
- [19] T. Ponnada, H. Al-Tous, O. Tirkkonen, and C. Studer, "An Out-of-Sample Extension for Wireless Multipoint Channel Charting," in *Cognitive Radio-Oriented Wireless Networks: 14th EAI International Conference, CrownCom 2019, Poznan, Poland, June 11–12, 2019, Proceedings 14*. Springer, 2019, pp. 208–217.
- [20] C. Geng, H. Huang, and J. Langerman, "Multipoint Channel Charting with Multiple-Input Multiple-Output Convolutional Autoencoder," in *2020 IEEE/ION Position, Location and Navigation Symposium (PLANS)*.
- [21] J. Pihlajasalo, M. Koivisto, J. Talvitie, S. Ali-Löytty, and M. Valkama, "Absolute Positioning with Unsupervised Multipoint Channel Charting for 5G Networks," in *2020 IEEE 92nd Vehicular Technology Conference (VTC2020-Fall)*. IEEE, 2020, pp. 1–5.
- [22] H. Al-Tous, P. Kazemi, C. Studer, and O. Tirkkonen, "Channel Charting with Angle-Delay-Power-Profile Features and Earth-Mover Distance," in *2022 56th Asilomar Conference on Signals, Systems, and Computers*, 2022, pp. 1195–1201.
- [23] J. B. Tenenbaum, V. d. Silva, and J. C. Langford, "A Global Geometric Framework for Nonlinear Dimensionality Reduction," *science*, vol. 290, no. 5500, pp. 2319–2323, 2000.
- [24] E. W. Dijkstra, "A Note on Two Problems in Connexion with Graphs," *Numer. Math.*, vol. 1, no. 1, p. 269–271, dec 1959.
- [25] J. B. Kruskal, "Multidimensional scaling by optimizing goodness of fit to a nonmetric hypothesis," *Psychometrika*, vol. 29, no. 1, 1964.
- [26] L. van der Maaten and G. Hinton, "Visualizing Data using t-SNE," *Journal of Machine Learning Research*, vol. 9, no. 86, 2008.
- [27] F. Schroff, D. Kalenichenko, and J. Philbin, "Facenet: A unified embedding for face recognition and clustering," *CoRR*, vol. abs/1503.03832, 2015.
- [28] J. Venna and S. Kaski, "Neighborhood preservation in nonlinear projection methods: An experimental study," in *International Conference on Artificial Neural Networks*. Springer, 2001, pp. 485–491.
- [29] C. Rajsiki, "A metric space of discrete probability distributions," *Information and Control*, vol. 4, no. 4, pp. 371–377, 1961.
- [30] F. Euchner, M. Gauger, S. Dörner, and S. ten Brink, "A Distributed Massive MIMO Channel Sounder for "Big CSI Data"-driven Machine Learning," in *WSA 2021; 25th International ITG Workshop on Smart Antennas*, 2021.
- [31] F. Euchner and M. Gauger, "CSI Dataset dichasus-cf0x: Distributed Antenna Setup in Industrial Environment, Day 1," 2022. [Online]. Available: <https://doi.org/doi:10.18419/darus-2854>